

Object Pose Estimation in Robotics Revisited

Antti Hietanen^{a,b,*}, Jyrki Latokartano^b, Alessandro Foi^a, Roel Pieters^b, Ville Kyrki^c, Minna Lanz^b, Joni-Kristian Kämäräinen^a

^a*Computing Sciences, Tampere University, Finland*

^b*Automation Technology and Mechanical Engineering, Tampere University, Finland*

^c*Department of Electrical Engineering and Automation, Aalto University, Finland*

Abstract

Vision-based object grasping and manipulation in robotics require accurate estimation of the object 6D pose. Therefore pose estimation has received significant attention and multiple datasets and evaluation metrics have been proposed. Most of the existing evaluation metrics rank the estimated poses solely based on the visual perspective i.e. how well two geometrical surfaces are aligned, which does not directly indicate the goodness of the pose for a robot manipulation. In robotic manipulation the optimal grasp pose depends on many factors such as target object weight and material, robot, gripper, and the task itself. In this work we address these factors by proposing a probabilistic evaluation metric that ranks an estimated object pose based on the conditional probability of completing a task given this estimated pose. The evaluation metric is validated in controlled experiments and a number of baseline and recent pose estimation methods are compared on a dataset of industrial parts for assembly tasks. The experimental results confirm that the proposed evaluation metric measures the fitness of an estimated pose more accurately for a robotic task compared to prior metrics.

Keywords: Grasping, 6D object pose, probabilistic models, cognitive robotics

2010 MSC: 00-01, 99-00

*Corresponding author. This project has received funding from the European Union's Horizon 2020 research and innovation programme under grant agreement No 825196.

1. Introduction

Robot grasping and manipulation are important building blocks in industrial manufacturing. In high-throughput assembly lines, fast and accurate grasping is established by custom-made bulk feeders [1]. However, feeders are unsuitable for low-volume production lines that require flexibility in task reconfiguration. Substantial research efforts have been devoted to bin picking and feeding, which is a more flexible and easily reconfigurable solution. Recent research suggests that it is possible to grasp a diverse set of objects from clutter using a robotic actuator that is guided by a deep convolutional neural networks (CNNs) trained on large datasets of grasp attempts on a simulator or a physical robot [2, 3, 4]. However, a successful grasp from a bin does not guarantee successful precision manipulation or wrenching and therefore specific methods have been proposed for certain tasks such as "peg-in-the-hole" [5]. General 6D object pose (3D translation and 3D rotation) estimation remains a challenging problem.

Vision-based object recognition and 6D pose estimation from RGB-D input have recently become an active research topic in computer vision [6, 7]. In a typical workflow, a method first recognizes the object in a scene using RGB input and then estimates and refines the pose using depth (D) which provides a 3D point cloud; the method output is a 6D object pose with respect to the world (robot) coordinate frame. The methods are trained and optimized using training samples with ground-truth pose annotations. Several 6D pose estimation datasets have been recently proposed [8, 9, 10, 11] for method comparison. The two most popular performance metrics are *average absolute translation/orientation error* and *average point cloud deviation error* between ground truth and estimated poses in a separate test set. A significant limitation of these metrics is that they effectively measure only the difference between two transformation matrices but this difference is not necessarily indicative of the success in any particular task with a real robot. The real success depends on many factors beyond the accuracy of estimating the 6D pose parameters: i) the manipulated object and its properties (material, weight, dimensions), ii) the

selected gripper (including fingers), iii) the selected grasp point and grasping maneuver, and iv) the task itself (bin picking vs. precision wrenching). There have been attempts to report success rates for a particular setup [12, 13, 14, 15], but these require implementation of the same physical setup for method evaluation. The robot-vision community would benefit from datasets and evaluation metrics that can measure the actual success in a specific task without requiring a physical setup.

The present work aims at providing such a dataset and metric. Specifically, we introduce a benchmark dataset and propose a performance metric for evaluating 6D pose estimation methods in robotics. The proposed benchmark does not require replication of the physical setup but is data-only yet providing evaluation with respect to specific tasks and a real setup. The training data consists of 3D point-cloud models of each object, whereas the test data consists of test scenes with various amounts of clutter and occlusions. For each object we provide a pre-computed conditional probability model that measures the success probability for a pose estimate (see Figure 1 for illustration). The metric is based on a probabilistic framework where the fitness of the estimated pose of an object is defined as the conditional probability, $P(X=1|\hat{\theta})$, of a successfully conducted task ($X=1$) given the estimated object pose $\hat{\mathbf{Y}}$ and its corresponding grasp point $\hat{\theta}$. A task is successful if moving the gripper to $\hat{\theta}$ and closing its fingers allows the robot to steadily lift up the work part and carry out the target task. Interpretation of the metric is therefore intuitive: 0.9 means that on average nine out of ten task attempts executed based on the estimated object pose will succeed.

Contributions. The main contributions of this work are:

- A statistical formulation of the conditional probability of a successful robotic operation given the estimated object pose $\hat{\mathbf{Y}}$. The given object pose is transformed to a grasp pose $\hat{\theta}$ defined in the object-relative coordinate space and evaluated using the proposed metric, i.e. $P(X=1|\hat{\theta})$. Here, the 6D pose vector $\hat{\theta} = (t_x, t_y, t_z, r_x, r_y, r_z)^T$ belongs to the 6D space

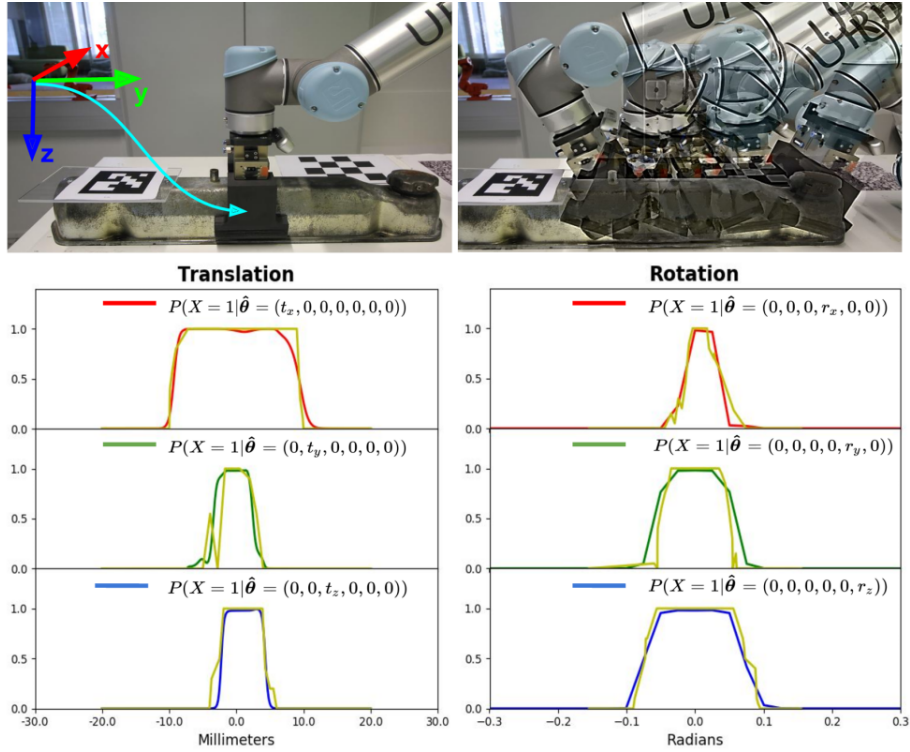


Figure 1: Engine cap used in our experiments. The coordinate system is object centric (top left) and pose samples are taken around a canonical grasp pose (see experiments for more details). Below are the estimated (the red, green and blue lines) and validated success probabilities (yellow line) on the six main axes (three translations and three rotations) in vicinity of the canonical grasp pose.

$\mathcal{E} = \mathbb{R}^3 \times S^3$, where S^3 denotes the 3D sphere parametrized by hyperspherical coordinates. The conditional grasp probability is implemented using non-parametric kernel regression on several random samples in \mathcal{E} .

- Procedures to generate semi-automatically a large number of random samples for estimating the grasp conditional probabilities. These procedures are exemplified in several setups where random samples are generated using a robot arm and industrial assembly tasks with different grippers and objects. The setups automatically evaluate the success of each grasp ($X = \{0, 1\}$) and are able to generate thousands of samples in 24 hours.

- A public benchmark for 6D object pose estimation in robotics. The benchmark consists of training point clouds, RGB-D test scenes, ground truth poses and pre-computed probability models for each object. In the experimental part of the work, the benchmark is used to evaluate several baseline and recent pose estimation methods.

All code and data will be made publicly available to facilitate fair comparisons and to promote similar dataset for other interesting tasks.

2. Related Work

Section 2.1 provides a brief review of the existing pose estimation datasets and their performance metrics, and Section 2.2 introduces popular baseline and more recent algorithms for 6D object pose estimation.

2.1. Benchmark datasets and performance metrics

Our main focus is on pose estimation from 3D data. 3D data is obtained, for example, using stereo, time-of-flight (ToF) or RGB-D (color + depth) sensors. The authors acknowledge that there are numerous works dealing with 3D recognition and pose estimation from 2D input such as gray level or color images. There are also many available "2D-to-3D" benchmark datasets such as Pascal3D [16]. However, for many robot manipulation applications and environments RGB is overly limited setting while 3D sensing can be readily adopted.

The early works evaluated methods with 3D object models from 3D scan datasets and generated synthetic scenes. A popular scan dataset is the Stanford 3D Scanning Repository [17] that contains, for example, the famous Stanford Bunny. For these datasets the typical performance metrics are *3D translation and 3D rotation errors* [18]. However, more recent works have attempted to combine the metrics to a single number.

One of the first real and still widely used 3D object recognition and 6D pose estimation datasets is LineMod introduced by Hinterstoisser et al. [11]. LineMod training data consists of 3D models and turn-table captured RGB and

depth images. The test data consists of various cluttered scenes that were captured from multiple view points on a turn-table. As a unified performance metric Hinterstoisser et al. proposed to use *average distance of corresponding model points* (ADC) which calculates the distance between model points transformed by the ground truth pose and the estimated pose. The metric is intuitive as it directly evaluates the fitness of the surface alignment. However the metric is not well defined for objects having symmetric properties since different poses may have similar displacement. To overcome this issue Hinterstoisser proposed a new similarity metric, where instead of calculating the distance between corresponding points the distance was measured between the closest pair of points.

Recently, Hodan et. al [8] introduced Benchmark for 6D Object Pose Estimation (BOP). BOP contains eight similarly captured datasets, including LineMod, that span various kinds of objects and scenes from household objects and scenes [19] to industrial [20]. Hodan et al. evaluated 15 recent methods on all eight datasets using a unified evaluation protocol. Their evaluation protocol takes into account view point dependent pose uncertainty and therefore they adopted the *Visible Surface Discrepancy* (VSD) [10] as the main error metric. VSD is invariant to pose ambiguity, i.e. due to the object symmetry there can be multiple poses that are indistinguishable. However the method requires additional ground truth in the form of visibility masks.

All above datasets and metrics measure the pose error as the misalignment between the ground truth and estimated object surface points. This requirement is important, for example, in augmented reality applications where the perceived virtual object must align well with the real environment. However, in robotic tasks, such as industrial assembly and disassembly, a performance metric should reflect the success in the task as proposed in this work.

2.2. 6D pose estimation methods

State-of-the-art methods divide RGB-D object pose estimation to two stages [7, 6]: i) detection of objects from RGB and ii) detected object pose estimation from depth (point cloud). Object detection is out of the scope of this work and there-

fore we briefly discuss the methods in the recent evaluation by Yang et al. [9] and who provide their code (note that NNSR is a robustified version of the SS baseline method).

Random Sample Consensus (RANSAC). RANSAC is a widely used technique for 6D pose estimation [21, 22, 23] adopted from the 2D domain. It is an iterative process that uses random sampling technique to generate candidate solutions for a model (transformation) that aligns two surfaces with a minimum point-wise error. Free parameter of the method is N_{RANSAC} which is the maximum count of pose hypothesis the algorithm samples matches from the correspondence set. The algorithm iteratively samples candidate transformations which are evaluated by transforming all the matched points and calculating the Euclidean distance between the corresponding points. All transformed point matches with distance less than d_{RANSAC} are counted as inliers. The final pose is estimated using all inlier points for transformation with the largest number of inliers.

Hough Transform (HG). Hough transform [24] is an alternative to RANSAC; instead of random samples each point match casts votes and pose with the largest number of votes is selected. There are several methods adopting this principle [25, 26] and for the experiments the Hough Grouping (HG) method by Tombari et al. [26] was selected. For fast computation, the method uses a unique model reference point (mass centroid) and bins represent pose around the reference point. To make correspondence points invariant to rotation and translation between the model and scene, every point is associated with a local reference frame [27]. The main parameter of the method is the pose bin size - coarse size provides faster computation but increases pose uncertainty.

Spectral Technique (ST). Leordeanu and Hebert [28] proposed a spectral grouping technique to find coherent clusters from the initial set of feature matches. The method takes into account the relationship between points and correspondences and finally uses an eigen-decomposition to estimate the confidence of a correspondence to be an inlier.

First the algorithm creates an affinity matrix \mathbf{M} which entries represent weighted links between correspondences. The weights are estimated by calculating the pairwise similarity between two correspondences using a rigidity constraint:

$$M(c_i, c_j) = \min \left\{ \frac{\|\mathbf{x}_i - \mathbf{x}_j\|}{\|\mathbf{x}'_i - \mathbf{x}'_j\|}, \frac{\|\mathbf{x}'_i - \mathbf{x}'_j\|}{\|\mathbf{x}_i - \mathbf{x}_j\|} \right\}, \quad (1)$$

where \mathbf{x} and \mathbf{x}' are the model and captured scene 3D points, respectively. The diagonal elements of the matrix measure the level of individual assignments i.e. how well f_i and f'_i match. After computing \mathbf{M} , the principle eigenvector \mathbf{v} of \mathbf{M} is calculated and the location of the maximum value v_i gives the highest confidence of c_i being in the inlier set. Next, all the correspondences conflicting with c_i are removed from the initial set of matches \mathbf{C} and procedure is repeated until $v_i = 0$ or \mathbf{C} is empty and finally the generated inlier set is returned.

Geometric Consistency (GC). While the RANSAC and Hough transform based methods operate directly on the 3D points there are methods that exploit the local neighborhood of points to establish more reliable matches between model and scene point clouds [29, 30]. Geometric Consistency Grouping (GC) [29] is a strong baseline and it has been implemented in several point cloud libraries. GC works independently from the feature space and utilizes only the spatial relationship of the corresponding points. The algorithm evaluates the consistency of two correspondences c_i and c_j using a compatibility score

$$d(c_i, c_j) = \left| \|\mathbf{x}_i - \mathbf{x}_j\| - \|\mathbf{x}'_i - \mathbf{x}'_j\| \right| < \tau_{GC} . \quad (2)$$

GC simply measures distances near the points and assigns correspondences to the same cluster if their geometric inconsistency is smaller than the threshold value τ_{GC} .

GC is initialized with a fixed number of clusters each having a seed correspondence. Then for each cluster it iteratively searches correspondences which satisfy the compatibility score (Eq. 2), mark them as visited and continue the process until all the correspondences are visited. Finally, all the cluster sets can be optionally refined using RANSAC. In principle, the GC algorithm can

return more than one cluster and for pose estimation the cluster with the largest number of correspondences is used as the pose estimate [31].

Search of Inliers (SI). A recent method by Buch et al. [30] achieves state-of-the-art on several benchmarks. It uses two consecutive processing stages, local voting and global voting. The first voting step performs local voting, where locally selected correspondence pairs are selected between a model and scene, and the score is computed using their pair-wise similarity score $s_L(c)$. At the global voting stage, the algorithm samples point correspondences, estimates a transformation and gives a global score to the points correctly aligned outside the estimation point set: $s_G(c)$. The final score $s(c)$ is computed by combining the local and global scores, and finally $s(c)$ are thresholded to inliers and outliers based on Otsu’s bimodal distribution thresholding.

3. Evaluating Object Pose in Robotics

A characteristic property of a vision guided robotic manipulation is that the probability of success in the task depends on the estimated object pose $\hat{\mathbf{Y}}$ which is then used to set the end effector location with respect to the manipulated object, i.e. the grasping point $\hat{\theta}$. The predefined grasp location on the object is carefully selected based on several different properties inherent to the task and even a slight deviation from this pose can result a unsuccessful operation attempt causing damage or major delays on the manufacturing line. In this section we propose a novel approach to evaluate an estimate of an object pose in terms of its effectiveness at completing a robotic manipulation task. The approach is based on a probabilistic model of successful object-relative grasp poses (3.1) and sampling the pose space to estimate the actual probability values (3.2). In the following sections we will use term pose instead of object-relative grasp pose.

3.1. Probability of completing a programmed task $P(X = 1)$

The success of a robot to complete its task is a binary random variable $X \in \{0, 1\}$ where $X = 1$ denotes a successful attempt and $X = 0$ denotes an

unsuccessful attempt (failure). Therefore, X follows the Bernoulli distribution, $P(X|p) = p^X(1-p)^{1-X}$, with complementary probability of success and failure: $E(X) = P(X=1) = 1 - P(X=0)$, where E denotes the mathematical expectation. The pose is defined by 6D pose coordinates $\boldsymbol{\theta} = (t_x, t_y, t_z, r_x, r_y, r_z)^T$ where the origin can be freely selected. The translation vector $(t_x, t_y, t_z)^T \in \mathbb{R}^3$ and 3D rotation $(r_x, r_y, r_z)^T \in SO(3)$ both have three degrees of freedom. The rotation is in axis-angle representation, where the length of the 3D rotation vector is the amount of rotations in radians, and the vector itself gives the axis about which to rotate. Adding pose to the formulation makes the success probability a conditional distribution and expectation a conditional expectation. The conditional probability of a successful attempt is

$$p(\boldsymbol{\theta}) = E(X|\boldsymbol{\theta}) = P(X=1|\boldsymbol{\theta}) = 1 - P(X=0|\boldsymbol{\theta}) . \quad (3)$$

The maximum likelihood estimate of the Bernoulli parameter $p \in [0, 1]$ from N homogeneous samples $y_i, i=1, \dots, N$, is the sample average

$$\hat{p}_{\text{ML}} = \frac{1}{N} \sum_{i=1}^N y_i , \quad (4)$$

where homogeneity means that all samples are realization of a common Bernoulli random variable with unique underlying parameter p . However, guaranteeing homogeneity would require that the samples $\{y_i, i=1, \dots, N\}$ were either all collected at the same pose $\boldsymbol{\theta}_1 = \dots = \boldsymbol{\theta}_N$, or for different poses that nonetheless yield same probability $p(\boldsymbol{\theta}_1) = \dots = p(\boldsymbol{\theta}_N)$, i.e. it would require us either to collect multiple samples for each $\boldsymbol{\theta} \in SE(3)$ or to know beforehand p over $SE(3)$ (which is what we are trying to estimate). This means that in practice p must be estimated from non-homogeneous samples, i.e. from $\{y_i, i=1, \dots, N\}$ sampled at pose $\{\boldsymbol{\theta}_i, i=1, \dots, N\}$ which can be different and having different underlying $\{p(\boldsymbol{\theta}_i), i=1, \dots, N\}$.

The actual form of p over $SE(3)$ is unknown and depends on many factors, e.g., the shape of an object, properties of a gripper and a task to be completed. Therefore it is not meaningful to assume any parametric shape such as the

Gaussian or uniform distribution. Instead, we adopt the Nadaraya-Watson non-parametric estimator which gives the *probability of a successful attempt* as

$$\hat{p}_{\mathbf{h}}(\boldsymbol{\theta}) = \frac{\sum_{i=1}^N y_i K_{\mathbf{h}}(\boldsymbol{\theta}_i - \boldsymbol{\theta})}{\sum_{i=1}^N K_{\mathbf{h}}(\boldsymbol{\theta}_i - \boldsymbol{\theta})}, \quad (5)$$

where $\boldsymbol{\theta}_i$ denotes the poses at which y_i has been sampled and $K_{\mathbf{h}} : \mathcal{E} \rightarrow \mathbb{R}^+$ is a non-negative multivariate kernel with vector scale $\mathbf{h} = (h_{t_x}, h_{t_y}, h_{t_z}, h_{r_x}, h_{r_y}, h_{r_z})^T > 0$.

In this work, $K_{\mathbf{h}}$ is the multivariate Gaussian kernel

$$\begin{aligned} K_{\mathbf{h}}(\boldsymbol{\theta}) &= G\left(\frac{t_x}{h_{t_x}}\right) G\left(\frac{t_y}{h_{t_y}}\right) G\left(\frac{t_z}{h_{t_z}}\right) \sum_{j \in \mathbb{Z}} G\left(\frac{r_x + 2j\pi}{h_{r_x}}\right) \cdot \\ &\quad \sum_{j \in \mathbb{Z}} G\left(\frac{r_y + 2j\pi}{h_{r_y}}\right) \sum_{j \in \mathbb{Z}} G\left(\frac{r_z + 2j\pi}{h_{r_z}}\right), \end{aligned} \quad (6)$$

where G is the standard Gaussian bell, $G(\theta) = (2\pi)^{-\frac{1}{2}} e^{-\frac{1}{2}\theta^2}$. The three sum terms in (6) realize the modulo- 2π periodicity of $SO(3)$.

The performance of the estimator (5) is heavily affected by the choice of \mathbf{h} , which determines the influence of samples y_i in computing $\hat{p}_{\mathbf{h}}(\boldsymbol{\theta})$ based on the difference between the estimated and sampled poses $\boldsymbol{\theta}$ and $\boldsymbol{\theta}_i$. Indeed, the parameter \mathbf{h} can be interpreted as reciprocal to the bandwidth of the estimator: too large \mathbf{h} results in excessive smoothing whereas too small results in localized spikes.

To find an optimal \mathbf{h} , we use the leave-one-out (LOO) cross-validation method. Specifically, we construct the estimator on the basis of $N-1$ training examples leaving out the i -th sample:

$$\hat{p}_{\mathbf{h}}^{\text{LOO}}(\boldsymbol{\theta}, i) = \frac{\sum_{j \neq i} y_j K_{\mathbf{h}}(\boldsymbol{\theta}_j - \boldsymbol{\theta})}{\sum_{j \neq i} K_{\mathbf{h}}(\boldsymbol{\theta}_j - \boldsymbol{\theta})}.$$

The likelihood of y_i given $\hat{p}_{\mathbf{h}}^{\text{LOO}}(\boldsymbol{\theta}_i, i)$ is either $\hat{p}_{\mathbf{h}}^{\text{LOO}}(\boldsymbol{\theta}_i, i)$ if $y_i = 1$, or $1 - \hat{p}_{\mathbf{h}}^{\text{LOO}}(\boldsymbol{\theta}_i, i)$ if $y_i = 0$. We then select \mathbf{h} that maximizes the total LOO log-likelihood over the whole set S_y :

$$\hat{\mathbf{h}} = \arg \max_{\mathbf{h}} \sum_{i|y_i=1} \log(\hat{p}_{\mathbf{h}}^{\text{LOO}}(\boldsymbol{\theta}_i, i)) + \sum_{i|y_i=0} \log(1 - \hat{p}_{\mathbf{h}}^{\text{LOO}}(\boldsymbol{\theta}_i, i)).$$

Our choices of the kernel and LOO optimization of the kernel parameters result to probability estimates that are verifiable by controlled experiments (as illustrated in Figure 1).

3.2. Sampling the pose space

Section 3.1 provides us a formulation of the probability of successful robotic manipulation given the object relative grasping point $P(X = 1|\theta)$. The practical realization of the probability values is based on Nadaraya-Watson non-parametric kernel estimator that requires a number of samples in various poses θ_i and information of success $y_i = 1$ or failure $y_i = 0$ for each attempt. For practical reasons we make the following assumptions:

- We define a canonical grasp pose respect to a manipulated object which is select based on the object intrinsic parameters (i.e. the distribution of mass) and task requirements (i.e. on which way the object is being installed). During the sampling procedure the canonical pose is located using a 2D marker.
- We sample the pose space around the canonical grasp pose, and therefore $\theta = (t_x, t_y, t_z, r_x, r_y, r_z)^T$ defines $SE(3)$ "displacement" from the canonical grasp pose. The robot task is programmed based on the canonical grasp pose and we can experimentally search limits for θ in which the task is guaranteed to fail (see Table 1). The intervals define maximum displacement for each of the independent pose component in which the task attempt can still succeed.

With the help of these assumptions we are able to define a sampling procedure that can record samples and their success or failures automatically.

2D markers. Automatic and accurate estimation of the object pose is realized by attaching 2D markers to the manipulated objects (see Figure 3 for an example). A camera is installed to the robot arm from where it can detect the 2D markers and provide accurate 6D poses using the ArUco library [32]. The library provides the Euclidean transformation from the detected marker to the sensor coordinate system $\mathbf{T}_{marker}^{sensor}$. In all coordinate transformations \mathbf{T}_B^A denotes a 4×4 rigid Euclidean transformation (isometry) matrix that describes

the position of the frame B origin and the orientation of its axes, relative to the reference frame A. All points are given in homogeneous coordinates $(x, y, z, 1)^T$.

Coordinate transformations. The world frame is fixed to the robot frame (i.e. center of the robot base) and programming is based on the tool point that is the end effector frame. All the required coordinate transformations in the sampling procedure are illustrated in Fig. 2. The coordinate transformation from the end effector frame to the world frame $\mathbf{T}_{effector}^{world}$ can be automatically calculated using the joint angles and known kinematic equations. Determining marker pose in the world frame is calculated using a carefully calibrated camera and by using the following transformation chain: $\mathbf{T}_{marker}^{world} = \mathbf{T}_{sensor}^{world} \cdot \mathbf{T}_{marker}^{sensor}$; and since the sensor is attached to the end effector $\mathbf{T}_{marker}^{world} = \mathbf{T}_{effector}^{world} \cdot \mathbf{T}_{sensor}^{effector} \cdot \mathbf{T}_{marker}^{sensor}$.

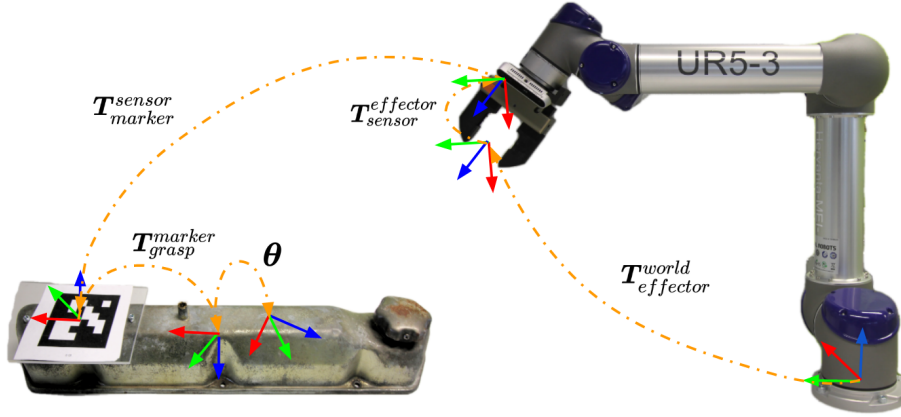


Figure 2: Coordinate frames used in random sampling of poses for assembly tasks.

The task starts by grasping the object. The canonical grasp pose is set to the position where the end effector does not move anymore but only closes its fingers. The end effector location at the grasp pose is measured with respect to the object (marker) via $\mathbf{T}_{grasp}^{marker}$ and this can be transformed to the world frame by using the transformation chain of $\mathbf{T}_{marker}^{world}$.

Finally, samples around the canonical grasp pose are generated from

$$\hat{\mathbf{T}}_{grasp}^{marker} = \mathbf{T}_{grasp}^{marker} \cdot \Phi(\theta) \quad (7)$$

where the operator $\Phi(\cdot)$ converts the 6D pose vector to a 4×4 matrix representation

$$\Phi(\theta) = \begin{bmatrix} \mathbf{R}_{3 \times 3} & \mathbf{t} \\ \mathbf{0} & 1 \end{bmatrix}. \quad (8)$$

The generated pose sample is defined in the vicinity of the canonical pose by the translation shift $\mathbf{t} = (t_x, t_y, t_z)^T$ and rotation matrix $\mathbf{R} \in \mathbb{R}^{3 \times 3}$ constructed from the axis-angle vector $(r_x, r_y, r_z)^T$. In summary, the transformation chain components are:

- $\mathbf{T}_{grasp}^{marker}$ – a constant transformation from the canonical grasp pose to the marker;
- $\mathbf{T}_{marker}^{sensor}$ – computed transformation from the marker to the sensor frame;
- $\mathbf{T}_{sensor}^{effector}$ – a constant transformation from the sensor frame to the robot end effector frame (camera is attached to the end effector);
- $\mathbf{T}_{effector}^{world}$ – computed transformation from the end effector to the world (robot origin).

$\mathbf{T}_{effector}^{world}$ is computed using the robot forward kinematics and $\mathbf{T}_{sensor}^{effector}$ is computed using the standard procedure for hand-camera calibration with a printed chessboard pattern [33]. For a calibrated camera the ArUco library provides an accurate real-time pose of the marker with respect to the world frame $\mathbf{T}_{marker}^{world}$. The constant offset from the marker to the actual grasp pose is computed from

$$\mathbf{T}_{grasp}^{marker} = \left(\mathbf{T}_{marker}^{world} \right)^{-1} \mathbf{T}_{grasp}^{world}.$$

where $\mathbf{T}_{grasp}^{world}$ is estimated manually by hand-guiding the end effector to the predefined grasp pose using the forward kinematics engine.

Detection of failures. Each of the work part has a predefined position and orientation how it should be installed, i.e. *ground truth installation pose*, respect to the target object. For instance most of the motor parts have to be placed on the motor block precisely in order to fasten the parts with screws. The robot task is to bring the part to this pose and finally release the part by opening the gripper fingers. In addition, using excessive force during the operation can cause

damage to the work objects. In the work there are two sources of information for detecting manipulation failures:

- too large difference between the installation pose of the manipulated object and the corresponding ground truth and
- too large wrench torque at the end effector at any moment of task execution (e.g. due to collisions), including grasping, carrying and installation.

Thresholds for the above are task specific and in our experiments they were manually set based on preliminary experiments.

For evaluation the success of the part installation in the terms of correct location the two thresholds are used: τ_t for the maximum translation error and τ_r for the maximum orientation error (both problem specific). These are computed using installation pose $\Upsilon = [\mathbf{R} \mid \mathbf{t}]$ measured using the marker attached to the manipulated work part and the ground truth installation pose $\hat{\Upsilon} = [\hat{\mathbf{R}} \mid \hat{\mathbf{t}}]$. Both are measured respect to the object on which the work part is being installed. The installation was successful if

$$\begin{aligned} \|\mathbf{t} - \hat{\mathbf{t}}\| &\leq \tau_t \\ \arccos\left(\frac{\text{trace}(\hat{\mathbf{R}}\mathbf{R}^{-1}) - 1}{2}\right) &\leq \tau_r \end{aligned} \quad (9)$$

The torque is used to detect if the robot collides with its environment during the task execution. In addition, if the robot places the object to the correct position with too high wrench the whole operation is considered as an unsuccessful attempt. The external wrench is computed based on the error between the joint torques required to stay on the programmed trajectory and the expected joint torques. The robot’s internal sensors provide the torque measurements $\mathbf{F} = (f_x, f_y, f_z)$, where f_x , f_y and f_z are the forces in the axes of the robot frame coordinates and measured in Newtons. For each task the limit f_{max} was manually set for each operation stage using preliminary experiments and violating the threshold, i.e $\|\mathbf{F}\| > f_{max}$, was recorded as failure. As a summary, all the step in the procedure all described in Alg. 1.

Algorithm 1: Sampling the pose space

Input: Robot program waypoints $\mathcal{W} := \{w_i | i = 1, \dots, N\}$; Number of samples S

Output: Set of samples $\{(\theta_i, y_i) | i = 1, \dots, S\}$

```
1 for  $i = 1$  to  $S$  do
2    $y_i \leftarrow$  success;
3    $\theta_i \leftarrow$  SampleRandomDisplacement();
4    $\mathbf{T}_{marker}^{sensor} \leftarrow$  DetectMarker( $\mathcal{W}$ );
5    $\mathbf{T}_{sensor}^{world} \leftarrow$  ComputeForwardKinematics();
   // end effector pose in object (marker) coordinate system
6    $\hat{\mathbf{T}}_{grasp}^{marker} \leftarrow$  SamplePose( $\theta_i, \mathbf{T}_{grasp}^{marker}$ );
   // end effector pose in world coordinate system
7    $\hat{\mathbf{T}}_{grasp}^{world} \leftarrow \mathbf{T}_{sensor}^{world} \cdot \mathbf{T}_{marker}^{sensor} \cdot \hat{\mathbf{T}}_{grasp}^{marker}$ ;
8   GraspObject( $\hat{\mathbf{T}}_{grasp}^{world}, \mathcal{W}$ );
9   if SuccessfulGrasp() is False then
10    // marker detected on the table or force limits exceeded
11     $y_i \leftarrow$  failure
12   else
13    InstallObject( $\mathcal{W}$ );
14    if SuccessfulInstall() is False then
15     // marker on wrong pose or force limits exceeded
16      $y_i \leftarrow$  failure
17   Record( $\theta_i, y_i$ );
18   MoveObjectToStart( $\mathcal{W}$ );
```

4. Experiments

We implement four assembly tasks for a robot arm and gripper and custom made fingers for the four objects that were manipulated in the tasks. The tasks, setups, experimental results and verification experiments are explained in the

following.

4.1. Tasks

To conduct experiments with tasks of sufficient practical relevance the tasks were inspired by the production line of a local engine manufacturing company. Three assembly tasks were selected from the line: (T1) installation of a motor cap 1, (T2) installation of a motor frame and (T3) installation of a motor cap 2 (different engine model). In addition, we defined a baseline (BL) task: picking and dropping a part to a container (the *faceplate* part from the Cranfield assembly benchmark). The tasks were programmed by an experienced engineer who also carefully selected the grippers and fingers. The engineer was instructed that a feeder with accurate pose is available. The tasks represent typical tasks in assembly lines.

4.2. Setup

In Figure 3 is illustrated the robotic setup used in our experiments. The setup consisted of a model 5 Universal Robot Arm (UR5) and a Schunk PGN-100 gripper. The gripper operates pneumatically and was configured to have a high gripping force (approximately 600N) to prevent object slippage. In addition, the gripper had custom 3D printed fingers plated with rubber. For visual perception, an Intel RealSense D415 RGB-D sensor was secured on a 3D printed flange mounted between the gripper and the robot end effector. All the in-house made 3D prints were made using nylon reinforced with carbon fiber to tolerate external forces during the experiments. All the computation was performed on a single laptop with Ubuntu 18.04.

4.3. Validation

All tasks and the canonical grasp poses were validated by executing the task 100 times with pose obtained using the 2D patterns (Section 3.2). No failures occurred during the validation. On average, successful executions took 45-55 seconds and in 24 hours the robot was able to execute approximately 1,100

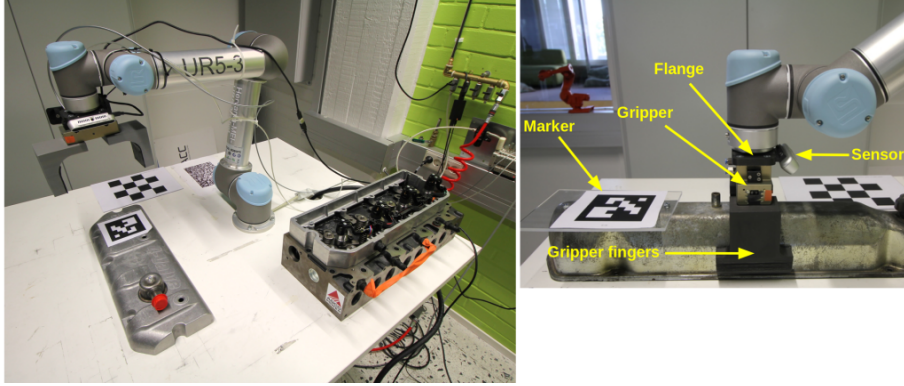


Figure 3: The experimental robot setup to sample the pose space of the engine cap 1. The task is to grasp and accurately assemble the cap to the engine mainframe.

attempts. The setup was able to automatically recover from most of the failure cases (dropping the object, object collision, etc.), however, if the marker was occluded by the environment or if the manipulated object got jammed against internal parts of the motor, the system was restarted by a human operator. For all tasks approximately 3,300 valid samples were generated.

4.4. RGB-D data capture

In the dataset each of the work part models are stored as a point cloud that represents a set of N 3D points $\{\mathbf{x}_i | i = 1, \dots, N\}$. In addition, for each point the corresponding color value $\mathbf{c} \in \mathbb{N}^3$ is stored. The models were generated using the same setup. The point cloud models were obtained automatically by moving the robot arm with the attached RGB-D sensor around each object. By using the camera poses obtained from robot kinematics the measurements were merged to a single point cloud that is the stored object model (see Fig. 4). The automatically captured point clouds were then manually checked and all artifacts and redundant parts of the reconstructed point cloud were removed manually using the open-source mesh processing software MeshLab [34].

The test dataset was generated in a similar manner by moving the arm around the work parts. For each of the objects 150 test images were collected

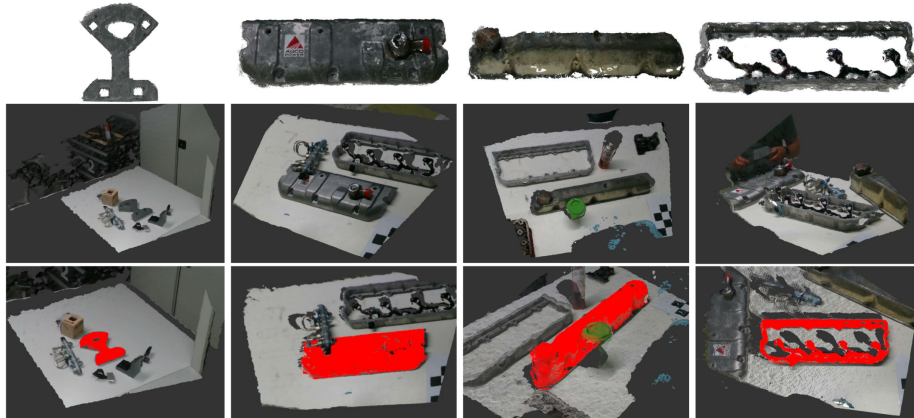


Figure 4: Top: Point cloud models of the used industry objects; faceplate, motor cap 1, motor cap 2 and a motor frame. The models were reconstructed by combining different view points of the robot arm and RGB-D sensor. Middle: example test samples (colored point clouds). Bottom: renderings of the object models on the test images using the ground truth poses.

in three different settings: 1) a single target object present, 2) multiple objects present and 3) the target object partially occluded by other object(s). The dataset contains manually verified ground truth to align the model point cloud to each test image and further to locate the canonical grasp pose relative to sensor (T_{sensor}^{grasp}).

4.5. Sampling

The probability model $P(X = 1|\theta)$ in Section 3.1 was generated using the sampling procedure in Section 3.2. Approximately 3,300 samples were used for each task. As defined in Section 3.2 the sampling was simplified by sampling translations and rotations around canonical grasp pose. The sampling procedure started by first finding the limits of the sampling in each dimension (a point after which execution always fails). The limits are shown in Table 1.

Validation. The estimated probability models were validated by sampling each dimension separately on grid points and executing the task ten times on each point with real robot. The averaged task success rate on real robot was then

Table 1: Sampling limits for translation (t_x, t_y, t_z) and rotation (r_x, r_y, r_z) in meters and degrees, respectively. Beyond these limits the task always fails.

	Motor cap	Motor frame	Motor cap 2	Cranfield top cap
t_x	$[-9.0, 9.0] \cdot 10^{-3}$	$[-6.0, 6.0] \cdot 10^{-3}$	$[-9.0, 9.0] \cdot 10^{-3}$	$[-6.5, 8.5] \cdot 10^{-3}$
t_y	$[-1.0, 1.0] \cdot 10^{-3}$	$[-3.0, 2.5] \cdot 10^{-3}$	$[-5.0, 6.0] \cdot 10^{-3}$	$[-2.1, 2.1] \cdot 10^{-2}$
t_z	$[-1.0, 5.0] \cdot 10^{-3}$	$[-2.0, 4.0] \cdot 10^{-3}$	$[-2.0, 5.0] \cdot 10^{-3}$	$[-1.2, 1.7] \cdot 10^{-2}$
r_x	$[-6.3, 6.3] \cdot 10^0$	$[-6.3, 6.3] \cdot 10^0$	$[-2.0, 1.0] \cdot 10^0$	$[-1.5, 1.5] \cdot 10^1$
r_y	$[-5.0, 5.0] \cdot 10^{-1}$	$[-2.5, 1.0] \cdot 10^0$	$[-2.0, 2.0] \cdot 10^0$	$[-1.5, 1.5] \cdot 10^1$
r_z	$[-5.0, 5.0] \cdot 10^{-1}$	$[-1.5, 1.5] \cdot 10^0$	$[-4.0, 4.0] \cdot 10^0$	$[-1.5, 1.5] \cdot 10^1$

compared against the proposed models and the estimated probabilities matched well as can be seen in Figure 1.

4.6. Methods

A method comparison was conducted for the methods described in Section 2.2. All selected algorithms use point clouds as inputs for the model and scene. The model and scene point clouds were downsampled to fixed resolutions using a regular voxel grid to limit the amount of data for processing. Depending on the density of the cloud the size of voxels was $0.5 - 1.0mm$. Since methods also exploit surface normals they were estimated using the standard least squares plane fitting on points in a small neighborhood. To further reduce the computational complexity in the matching stage, we avoid using all the surface points as local keypoints and only select a uniform subset of $1000 - 3000$ points per object model using the voxel grid filtering. Finally, local descriptors for point matching were computed using the local point neighborhoods. The SHOT [27] feature descriptor was selected since it performed the best in the preliminary experiments. The descriptor support radius was set to $0.125 \times$ the object model’s minimal bounding box diagonal. For each test scene, the best matching descriptors in L_2 sense between the model and scene were selected using a randomized kd -tree similarity search. The best matches formed then

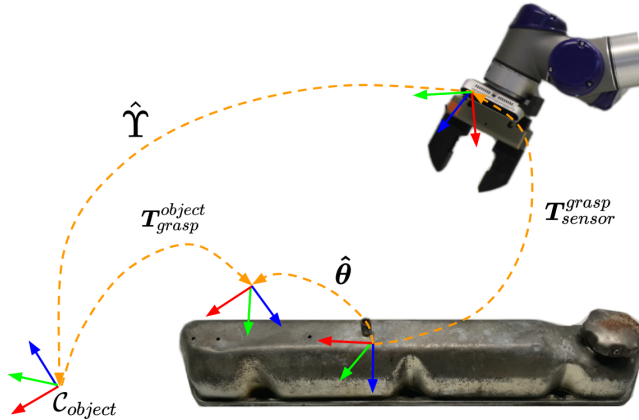


Figure 5: Coordinate frames in the evaluation procedure.

the initial set of correspondences for each method.

4.7. Performance indicators


The main performance metric in our work is the estimated success probability defined in Section 3.1. The probabilities were computed around the canonical grasp pose of each object and therefore the sampled values actually represent residual from this pose (see Fig. 5). The corresponding object-relative grasp pose of the pose estimate $\hat{\mathbf{Y}}$ is calculated as:


$$\hat{\boldsymbol{\theta}} = \Phi^{-1}(\mathbf{T}_{sensor}^{grasp} \hat{\mathbf{Y}} \mathbf{T}_{grasp}^{object}) , \quad (10)$$

where the transformation matrices $\mathbf{T}_{sensor}^{grasp}$ and $\mathbf{T}_{grasp}^{object}$ define the canonical grasp pose respect to the sensor and object (model) coordinate system, respectively. The $\Phi^{-1}(\cdot)$ operator converts the 4×4 pose matrix to 6D vector representation. Finally, the task success is evaluated using the proposed metric as $P(X=1|\hat{\boldsymbol{\theta}})$. We calculated the average probabilities over the whole dataset and also the proportion of images for which the probability is greater or equal to 0.90.

In addition to the proposed indicator we also report the ADC (Average Distance of Corresponding Model Point) error calculated over the points transformed by the ground truth and estimated object pose as suggested in [11]. The

Table 2: Comparison of pose estimation methods with our dataset (single: single object in the scene; multi: multiple objects (clutter); occ: multiple objects and occlusion; all: average over all test samples).

Part: <i>Motor cap</i> ; Gripper: <i>Shunker</i> Fingers: <i>Custom made</i>														Part: <i>Motor frame</i> ; Gripper: <i>Shunker</i> Fingers: <i>Custom made</i>													
																											
Avg Prob. $p(\cdot)$					ADC				Avg Prob. $p(\cdot)$					ADC													
single	multi	occ	all	≥ 0.9	all	top-25%	single	multi	occ	all	≥ 0.9	all	top-25%	single	multi	occ	all	≥ 0.9	all	top-25%							
GC [29]	0.24	0.18	0.12	0.19	12%	0.08	$3.83 \cdot 10^{-3}$	0.21	0.22	0.19	0.21	9%	0.02	$5.36 \cdot 10^{-3}$													
HG [26]	0.31	0.29	0.20	0.26	14%	0.06	$3.87 \cdot 10^{-3}$	0.28	0.27	0.27	0.28	15%	0.03	$5.19 \cdot 10^{-3}$													
SI [30]	0.00	0.00	0.00	0.00	0%	0.46	$1.78 \cdot 10^{-1}$	0.14	0.04	0.03	0.07	5%	0.42	$1.81 \cdot 10^{-2}$													
ST [28]	0.01	0.03	0.00	0.01	0%	0.35	$9.12 \cdot 10^{-2}$	0.23	0.16	0.07	0.17	7%	0.34	$4.38 \cdot 10^{-3}$													
NNSR [24]	0.00	0.00	0.00	0.00	0%	0.26	$1.18 \cdot 10^{-1}$	0.00	0.00	0.00	0.00	0%	0.36	$1.50 \cdot 10^{-1}$													
RANSAC [21]	0.00	0.00	0.00	0.00	0%	0.75	$1.71 \cdot 10^{-1}$	0.00	0.00	0.00	0.00	0%	0.65	$2.03 \cdot 10^{-1}$													

Part: <i>Motor cap v2</i> ; Gripper: <i>Shunker</i> Fingers: <i>Custom made</i>														Part: <i>Cranfield faceplate</i> ; Gripper: <i>Shunker</i> Fingers: <i>Custom made</i>													
																											
Avg Prob. $p(\cdot)$					ADC				Avg Prob. $p(\cdot)$					ADC													
single	multi	occ	all	≥ 0.9	all	top-25%	single	multi	occ	all	≥ 0.9	all	top-25%	single	multi	occ	all	≥ 0.9	all	top-25%							
GC [29]	0.24	0.25	0.20	0.24	13%	0.09	$6.28 \cdot 10^{-3}$	0.66	0.67	0.59	0.64	65%	0.15	$4.57 \cdot 10^{-3}$													
HG [26]	0.13	0.21	0.10	0.15	9%	0.11	$7.81 \cdot 10^{-3}$	0.64	0.68	0.56	0.63	60%	0.16	$3.43 \cdot 10^{-3}$													
SI [30]	0.11	0.19	0.11	0.13	8%	0.09	$1.11 \cdot 10^{-2}$	0.37	0.43	0.20	0.35	35%	0.39	$9.94 \cdot 10^{-3}$													
ST [28]	0.17	0.18	0.08	0.15	8%	0.11	$5.46 \cdot 10^{-3}$	0.40	0.39	0.30	0.37	36%	0.30	$6.47 \cdot 10^{-3}$													
NNSR [24]	0.02	0.00	0.00	0.01	1%	0.19	$6.10 \cdot 10^{-2}$	0.05	0.04	0.07	0.05	5%	0.28	$7.16 \cdot 10^{-2}$													
RANSAC [21]	0.00	0.00	0.00	0.00	0%	0.28	$1.24 \cdot 10^{-1}$	0.00	0.04	0.00	0.01	1%	0.51	$1.05 \cdot 10^{-1}$													

ADC error is computed from

$$\epsilon_{ADC} = \frac{1}{|\mathcal{M}|} \sum_{\mathbf{x} \in \mathcal{M}} \left\| \hat{\mathbf{Y}}\mathbf{x} - \mathbf{Y}\mathbf{x} \right\| \quad (11)$$

where \mathcal{M} is the set of all points in the each model. We also report the top-25% ADC error, which is less affected by outliers.

4.8. Results

The results for all methods and parts are in Table 2. The two best methods are Hough Transform (HG) by Tombari et al. [26] and GC by Chen and

Bhanu [29]. HG and GC perform considerably better than the two more state-of-the-art methods SI and ST although the performance of all methods remains surprisingly low. The two baselines, simple Hough voting (NNSR) and RANSAC, perform poorly.

Success probability vs. ADC. It is important to notice that the ADC results indicate much smaller difference between the methods than the success probability despite the fact that success probability directly measures success in the task. The reason is evident in Figure 6 where the ADC errors and success probabilities are plotted in the same graph. It is obvious that for ADC (green dots) there are clear points after which the success probability drops from close to 1.0 to almost 0.0. Therefore, ADC which provides a linear scale poorly ranks pose estimation methods for robot manipulation. This non-linear behavior between ADC and success probability was verified in a controlled experiment illustrated in Figure 7.

5. Conclusions

This work revisited evaluation of vision based object pose estimation methods for robotics. We quantitatively demonstrated how the popular error measures such as Average Distance of Corresponding Model Points (ADC), cannot indicate when the estimated pose will result to a task failure and thus becomes uninformative. As a novel solution, we proposed a statistical formulation of the success probability given an estimated object pose and used the formulation to evaluate a number of popular pose estimation methods. Notably, the novel metric and dataset provide basis for more realistic evaluation of object pose estimation methods without requiring a physical setup. We will make all code and data available to facilitate fair comparisons and to boost object pose estimation research in the robotics and computer vision communities.

References

References

- [1] V. Limere, H. V. Landeghema, M. Goetschalckx, E.-H. Aghezzafa, L. McGinnis, Optimising part feeding in the automotive assembly industry: deciding between kitting and line stocking, *International Journal of Production* 50 (15).
- [2] K. Bousmalis, A. Irpan, P. W. Y. Bai, M. Kelcey, M. Kalakrishnan, L. Downs, J. Ibarz, P. Pastor, K. Konolige, S. Levine, V. Vanhoucke, Using simulation and domain adaptation to improve efficiency of deep robotic grasping, in: *ICRA*, 2018.
- [3] J. Mahler, K. Goldberg, Learning deep policies for robot bin picking by simulating robust grasping sequences, in: *CoRL*, 2018.
- [4] S. Levine, P. Pastor, A. Krizhevsky, J. Ibarzland, D. Quillen, Learning hand-eye coordination for robotic grasping with deep learning and large-scale data collection, *International Journal of Robotics Research* 37 (4-5).
- [5] S.-K. Yun, Compliant manipulation for peg-in-hole: is passive compliance a key to learn contact motion?, in: *ICRA*, 2008.
- [6] F. Manhardt, W. Kehl, N. Navab, F. Tombari, Deep model-based 6d pose refinement in rgb, in: *ECCV*, 2018.
- [7] W. Kehl, F. Manhardt, F. Tombari, S. Ilic, N. Navab, Ssd-6d: Making rgb-based 3d detection and 6d pose estimation great again, in: *ICCV*, 2017.
- [8] T. Hodan, F. Michel, E. Brachmann, W. Kehl, A. GlentBuch, D. Kraft, B. Drost, J. Vidal, S. Ihrke, X. Zabulis, et al., Bop: benchmark for 6d object pose estimation, in: *ECCV*, 2018, pp. 19–34.
- [9] J. Yang, K. Xian, Y. Xiao, Z. Cao, Performance evaluation of 3d correspondence grouping algorithms, in: *3DV*, IEEE, 2017, pp. 467–476.

- [10] T. Hodaň, J. Matas, Š. Obdržálek, On evaluation of 6d object pose estimation, in: ECCV, Springer, 2016, pp. 606–619.
- [11] S. Hinterstoisser, V. Lepetit, S. Ilic, S. Holzer, G. Bradski, K. Konolige, N. Navab, Model based training, detection and pose estimation of textureless 3d objects in heavily cluttered scenes, in: ACCV, Springer, 2012, pp. 548–562.
- [12] U. Viereck, A. t. Pas, K. Saenko, R. Platt, Learning a visuomotor controller for real world robotic grasping using simulated depth images, arXiv preprint arXiv:1706.04652.
- [13] M. Gualtieri, A. Ten Pas, K. Saenko, R. Platt, High precision grasp pose detection in dense clutter, in: IROS, IEEE, 2016, pp. 598–605.
- [14] L. Pinto, A. Gupta, Supersizing self-supervision: Learning to grasp from 50k tries and 700 robot hours, in: ICRA, IEEE, 2016, pp. 3406–3413.
- [15] A. Saxena, L. Wong, M. Quigley, A. Y. Ng, A vision-based system for grasping novel objects in cluttered environments, in: Robotics research, Springer, 2010, pp. 337–348.
- [16] Y. Xiang, R. Mottaghi, S. Savarese, Beyond pascal: A benchmark for 3d object detection in the wild, in: IEEE Winter Conference on Applications of Computer Vision (WACV), 2014.
- [17] G. Turk, M. Levoy, Zippered polygon meshes from range images, in: SIGGRAPH, 1994.
- [18] J. Shotton, B. Glocker, C. Zach, S. Izadi, A. Criminisi, A. Fitzgibbon, Scene coordinate regression forests for camera relocalization in rgb-d images, in: CVPR, 2013, pp. 2930–2937.
- [19] A. Doumanoglou, R. Kouskouridas, S. Malassiotis, T.-K. Kim, Recovering 6d object pose and predicting next-best-view in the crowd, in: CVPR, 2016, pp. 3583–3592.

- [20] T. Hodan, P. Haluza, Š. Obdržálek, J. Matas, M. Lourakis, X. Zabulis, T-less: An rgb-d dataset for 6d pose estimation of texture-less objects, in: WACV, IEEE, 2017, pp. 880–888.
- [21] M. A. Fischler, R. C. Bolles, Random sample consensus: a paradigm for model fitting with applications to image analysis and automated cartography, *Communications of the ACM* 24 (6) (1981) 381–395.
- [22] E. Brachmann, A. Krull, F. Michel, S. Gumhold, J. Shotton, C. Rother, Learning 6d object pose estimation using 3d object coordinates, in: ECCV, Springer, 2014, pp. 536–551.
- [23] E. Brachmann, F. Michel, A. Krull, M. Yang, S. Gumhold, C. Rother, Uncertainty-driven 6d pose estimation of objects and scenes from a single RGB, in: CVPR, 2016.
- [24] P. V. Hough, Method and means for recognizing complex patterns, uS Patent 3,069,654 (Dec. 18 1962).
- [25] J. Knopp, M. Prasad, G. Willems, R. Timofte, L. van Gool, Hough transform and 3D SURF for robust three dimensional classification, in: ECCV, 2010.
- [26] F. Tombari, L. Di Stefano, Object recognition in 3d scenes with occlusions and clutter by hough voting, in: PSIVT, IEEE, 2010, pp. 349–355.
- [27] F. Tombari, S. Salti, L. Di Stefano, Unique signatures of histograms for local surface description, in: ECCV, Springer, 2010, pp. 356–369.
- [28] M. Leordeanu, M. Hebert, A spectral technique for correspondence problems using pairwise constraints, in: Tenth IEEE International Conference on Computer Vision (ICCV’05) Volume 1, Vol. 2, IEEE, 2005, pp. 1482–1489.
- [29] H. Chen, B. Bhanu, 3d free-form object recognition in range images using local surface patches, *Pattern Recognition Letters* 28 (10) (2007) 1252–1262.

- [30] A. Glent Buch, Y. Yang, N. Kruger, H. Gordon Petersen, In search of inliers: 3d correspondence by local and global voting, in: CVPR, 2014, pp. 2067–2074.
- [31] A. Hietanen, J. Halme, A. G. Buch, J. Latokartano, J.-K. Kämäräinen, Robustifying correspondence based 6D object pose estimation, in: IEEE Int. Conf. on Robotics and Automation (ICRA), Singapore, 2017.
- [32] S. Garrido-Jurado, R. Muñoz-Salinas, F. J. Madrid-Cuevas, M. J. Marín-Jiménez, Automatic generation and detection of highly reliable fiducial markers under occlusion, *Pattern Recognition* 47 (6) (2014) 2280–2292.
- [33] F. C. Park, B. J. Martin, Robot sensor calibration: solving $ax=xb$ on the euclidean group, *IEEE Transactions on Robotics and Automation* 10 (5) (1994) 717–721.
- [34] P. Cignoni, M. Callieri, M. Corsini, M. Dellepiane, F. Ganovelli, G. Ranzuglia, Meshlab: an open-source mesh processing tool., in: *Eurographics Italian chapter conference*, Vol. 2008, 2008, pp. 129–136.

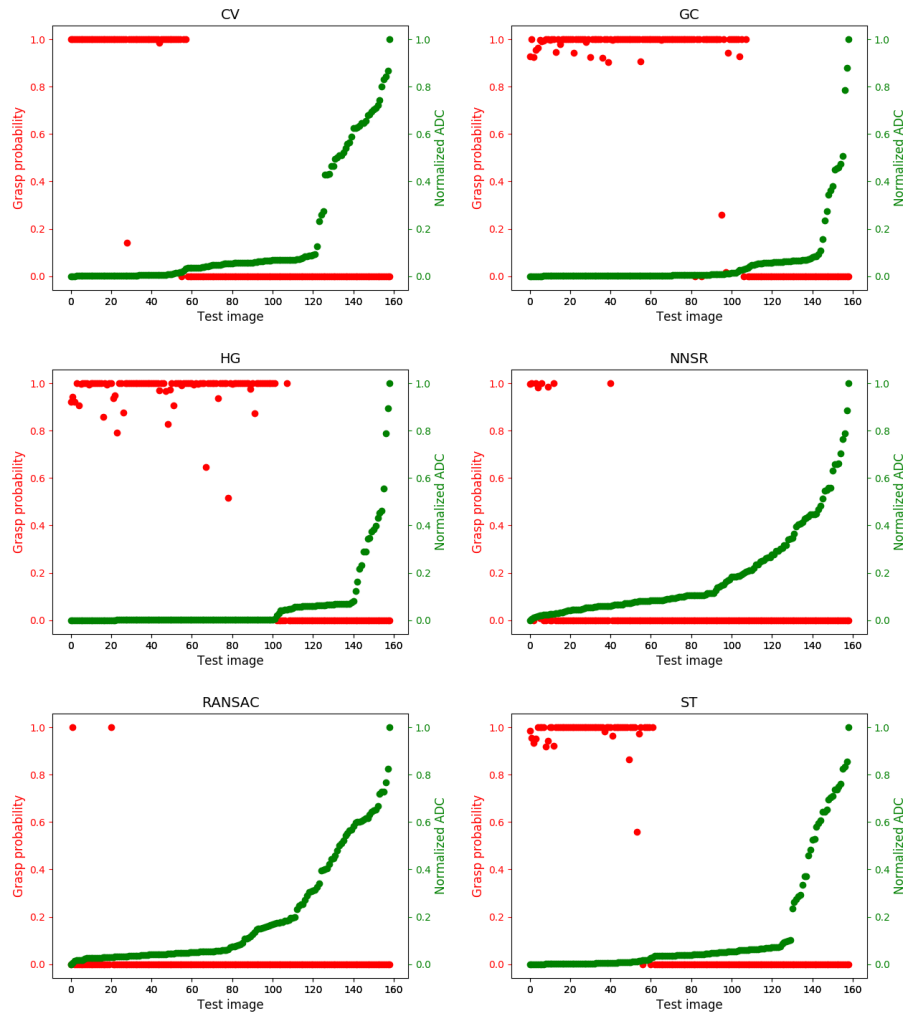


Figure 6: ADC pose error (green) and success probability (red) of all test samples of the Cranfield faceplate object for different pose estimation methods. Samples sorted based on their ADC error. Note rapid change from success (1.0) to failure (0.0) when the error goes beyond certain points.

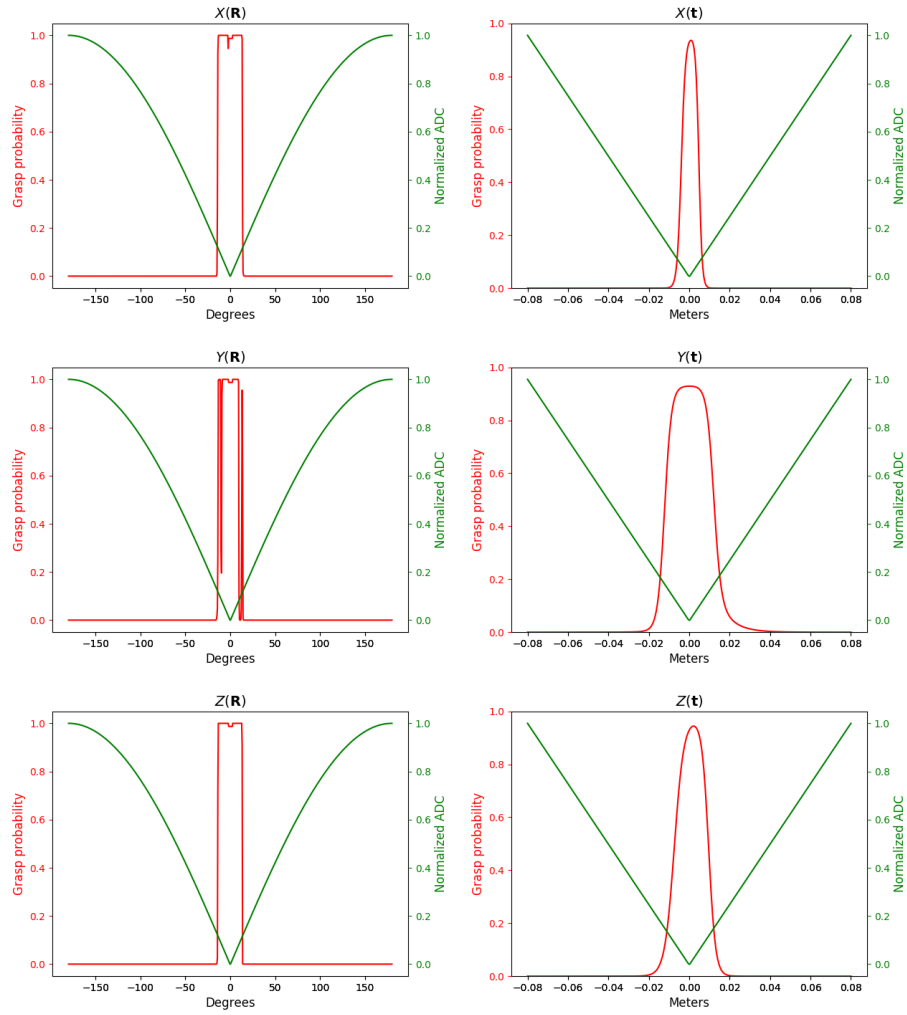


Figure 7: ADC and success probability from controlled experiments (Cranfield faceplate). Effect of rotation (left column) and translation (right column) to the ADC and success probability.